

AlGaN/AlN heterostructures: an emerging platform for nonlinear integrated photonics

Sinan Gündoğdu,^{1,2,*} Sofia Pazzagli,¹ Tommaso Pregolato,^{1,2} Tim Kolbe,² Sylvia Hagedorn,² Markus Weyers,² and Tim Schröder^{1,2}

¹*Department of Physics, Humboldt-Universität zu Berlin, Newtonstr. 15, 12489 Berlin, Germany*

²*Ferdinand-Braun-Institut (FBH), Gustav-Kirchhoff-Str. 4, 12489 Berlin, Germany*

(Dated: May 3, 2024)

In the rapidly evolving area of integrated photonics, there is a growing need for materials that satisfy the particular requirements of increasingly complex and specialized devices and applications. Present photonic material platforms have made significant progress over the past years; however, each platform still faces specific material and performance challenges. We introduce a novel material for integrated photonics: Aluminum Gallium Nitride (AlGaN) on Aluminum Nitride (AlN) as a platform for developing reconfigurable and nonlinear on-chip optical systems. AlGaN combines compatibility with standard semiconductor fabrication technologies, high electro-optic modulation capabilities, and large nonlinear coefficients while providing a broad and low-loss spectral transmission range, making it a viable material for advanced photonic applications. In this work, we design and grow AlGaN/AlN heterostructures and integrate fundamental photonic building blocks into these chips. In particular, we fabricate edge couplers, low-loss waveguides, directional couplers, and tunable high-quality factor ring resonators to enable nonlinear light-matter interaction and quantum functionality. The comprehensive platform we present in this work paves the way for nonlinear photon-pair generation applications, on-chip nonlinear quantum frequency conversion, and fast electro-optic modulation for switching and routing classical and quantum light fields.

I. INTRODUCTION

Advanced classical and quantum photonic applications, such as photonic neuromorphic computing [1], quantum sensing [2] and quantum networking [3–7] rely on photonic integrated circuits that enable the compact, efficient, and high-rate implementation of a variety of optical functionalities. In addition to functionalities adapted from stand-alone optical devices, integrated circuits provide access to mode-multiplexing or routing [8, 9] and efficient fiber coupling. A comprehensive photonic device platform [10], therefore, integrates various components, such as low-loss waveguides, efficient directional couplers, spectral filters, and tunable Mach-Zehnder interferometers (Fig. 1). A tunable ring resonator is another particularly versatile component, which can be employed to spectrally filter different modes, to enhance light-matter interaction, or to enable nonlinear frequency conversion and photon-pair generation.[11–13]. Additionally, given the large variety of electronic and optical components readily available on different material platforms, like detectors [14, 15] or quantum light sources [16, 17], heterogenous integration is a key approach for building photonic integrated chips with a high level of complexity. An ideal photonic platform should, therefore, facilitate such a method while also exhibiting properties such as low optical losses, fast electro-optic modulation, and significant optical nonlinearities to route and manipulate the propagating photons with high efficiency.

Different material platforms are currently being stud-

ied, each with its own advantages and disadvantages in meeting the requirements of a versatile, scalable, and reliable photonic platform. For the ultraviolet and visible spectral range, there are several established alternatives to silicon, which is not transparent in this range. Lithium niobate on insulator (LNOI) is one of the leading platforms due to its outstanding electro-optic coefficient, high optical nonlinearity, and recent progress in technological development [18–21]. However, LNOI faces several challenges. Non-standard etching processes are needed to fabricate optical components. These processes are incompatible with the conventional manufacturing standards, potentially hindering its scalability [22]. Moreover, despite the advances in epitaxial techniques, research, and industry still predominantly rely on smart-cut lithium niobate derived from bulk crystals, which typically suffer from crystal damage. Furthermore, the limited thickness range (>300 nm) of smart-cut lithium niobate restricts some applications, such as nanoscale integrated optics [23].

Silicon nitride (SiN), another established material platform, offers low losses [24] and is compatible with silicon manufacturing standards. SiN-based active optical elements, however, such as tunable Mach-Zehnder Interferometers (MZIs), typically rely on thermo-optic modulation due to their limited electro-optic functionality [25]. Thermo-optic control is comparably slow and generally limited to kHz modulation rates [26]. Another nitride-based material, aluminum nitride (AlN) on sapphire, has been explored due to its substantial nonlinear coefficient, its broad transparency range, and its moderate electro-optic coefficient [27–31]. AlN on sapphire, however, has yet other limitations. It is usually grown by sputtering or metal-organic vapor phase epitaxy (MOVPE), typically

* sinang@physik.hu-berlin.de

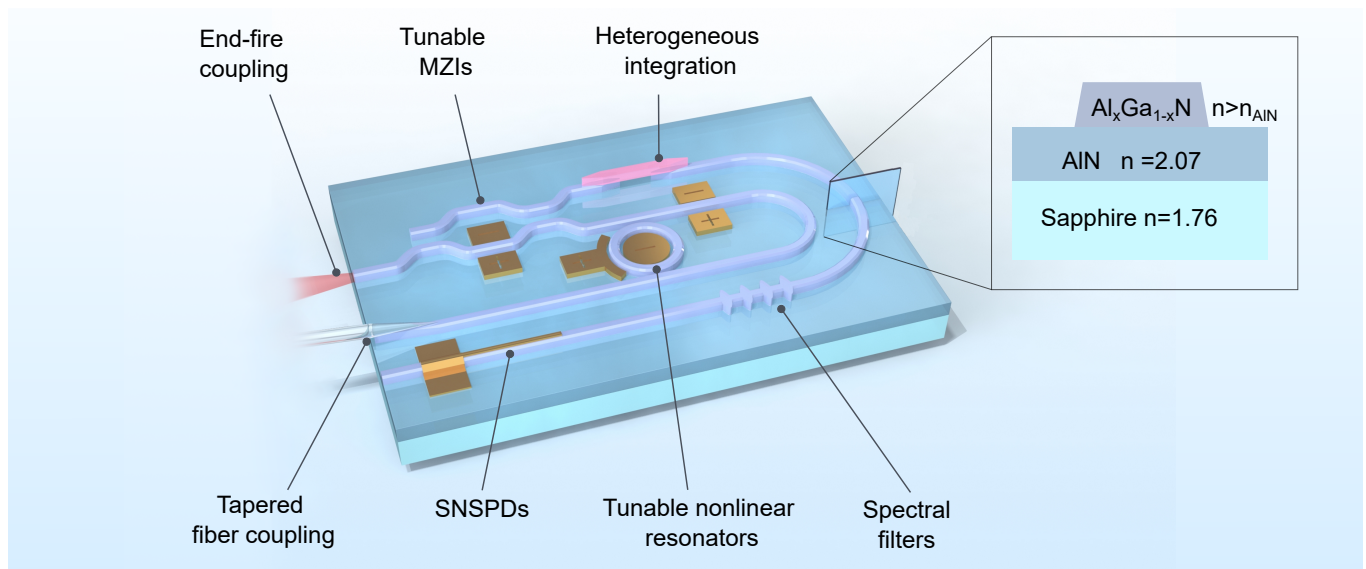


FIG. 1. **Illustration of AlGaIn/AIn platform for photonic integrated circuits.** The AlGaIn/AIn platform consists of various passive and active components. The core innovation is the photonic layer in which light is guided by engineering a few hundred-nanometer-thick high refractive index top layers, separating the optical mode from the sapphire substrate interface. Through lateral patterning, a large variety of passive and active optical elements can be integrated, including waveguides, directional couplers, tunable Mach-Zehnder interferometers, microring resonators as spectral filters and nonlinear devices, photonic crystals, and superconducting nanowire single-photon detectors. Additionally, this platform allows for the heterogeneous integration of functional electronic and optically active components, such as laser diodes, and solid-state quantum light sources, such as defects in diamonds and fluorescent molecules in organic matrices.

on a sapphire substrate. Consequently, the AlN layer suffers from a high defect density at the sapphire interface [32–34], which leads to relatively high optical scattering and absorption losses. Furthermore, commercially available AlN suffers from non-negligible thickness variation, making it challenging to fabricate photonic components scalably.

In this study, we introduce a platform for photonic integrated circuits based on aluminum gallium nitride (AlGaIn), where the AlGaIn layer acts as a guiding photonic layer that can be patterned into a large variety of optical components. This approach overcomes challenges in AlN on sapphire platforms, such as crystal defects at the sapphire-AlN interface and lateral thickness variation, and introduces further material-specific functionality. With the additional AlGaIn layer, we reduce optical losses and improve device performance compared to AlN on sapphire by shifting the optical mode away from this interface. The ability to control the ratio of aluminum to gallium in the ternary alloy $\text{Al}_x\text{Ga}_{1-x}\text{N}$ allows for tailored properties of the photonic layer, such as bandgap and refractive index engineering. Moreover, AlGaIn’s wide band gap enables efficient light transmission across a broad spectrum, depending on composition from below 250 nm to long-wave infrared. Doping AlGaIn for electrical conductivity combines optical and electronic functionalities, enabling, for example, current-induced refractive index change [35, 36].

Our AlGaIn platform benefits from the advanced

state-of-the-art of GaN, which has, over the past decade, evolved into a foundational material for electronic and electro-optic devices, including power electronics and light generation [37, 38]. For example, GaN LEDs and lasers are widely used for producing blue and green light [39, 40]. The epitaxial growth of GaN/AlGaIn/InGaIn heterostructures on sapphire templates, a well-established practice, opens up possibilities for integrating light sources and electronics on the photonic platform.

The inherent properties of AlGaIn, such as its relatively high electro-optic coefficient [41, 42], make it an ideal candidate for rapid modulation and the development of reconfigurable optical devices. Its significant second-order optical nonlinearity paves the way for on-chip nonlinear photonic devices, including parametric oscillators and sum or difference frequency generators. The generation of correlated photon pairs in the ultraviolet (UV) and visible spectrum has been proposed using an AlGaIn/AIn integrated photonics platform via spontaneous four-wave mixing (SFWM) in an AlGaIn microring resonator [43]. AlGaIn has also been explored as a potential platform for stimulated Brillouin scattering devices such as a racetrack Brillouin laser [44].

To the best of our knowledge, only very few studies have used AlGaIn as a photonic material. Li et al. [45] fabricated large, multimode waveguides with an AlN/GaN multiple quantum well core and $\text{Al}_{0.1}\text{Ga}_{0.9}\text{N}$ claddings. Although this is a notable achievement, the

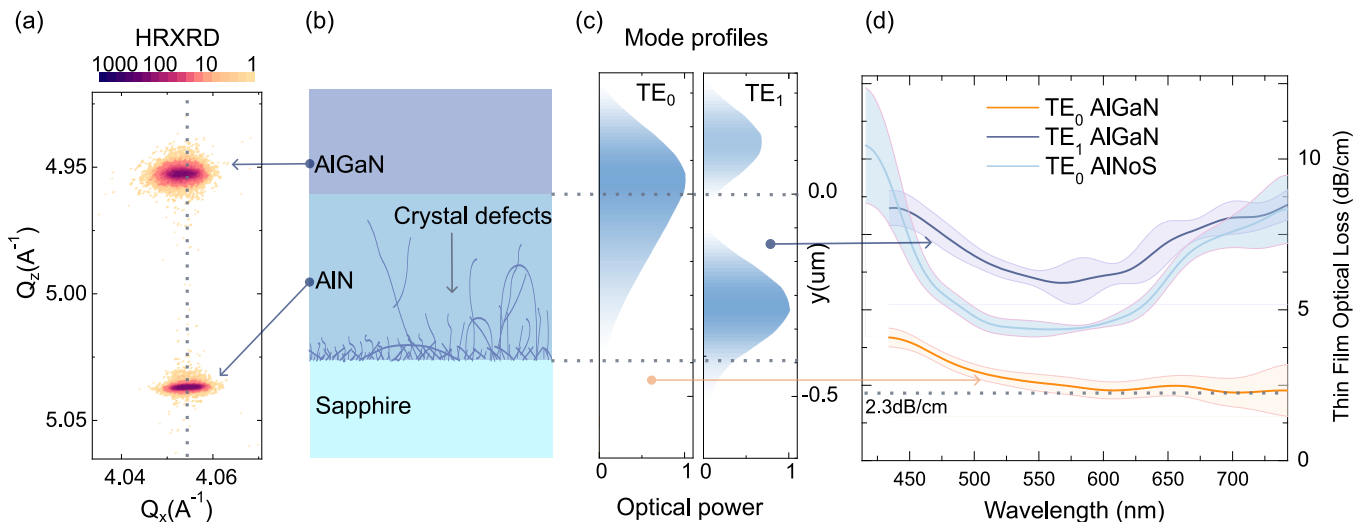


FIG. 2. **Material characterization.** (a) High-resolution X-ray diffraction reciprocal space maps (11-24 reflection) illustrate the strain relaxation in the AlGaIn and AlN layers. Two distinct peaks correspond to the AlN and AlGaIn layers, respectively. Analysis of these peaks reveals an Al-mole fraction $x = 0.69$ and a mere 3% relaxation of in-plane compressive strain in the AlGaIn layer, indicating a predominantly pseudomorphic growth on the AlN template and avoiding the generation of strain-relief defects. (b) Illustration of the basic heterostructure on a sapphire substrate. (c) Supported TE_0 and TE_1 modes for a 250 nm thick AlGaIn layer on AlN at 632 nm. (d) The optical loss spectrum of these modes in the AlGaIn/AlN heterostructure and the TE_0 mode of a 0.4 μm thick AlN single layer on sapphire film (AlNoS), measured by prism coupling, where shaded areas indicate the uncertainty bounds.

large size and relatively high sidewall roughness do not enable application for single-mode photonics. In addition, the wavelength range is limited to around 350 nm and longer. Bruch et al. [46] fabricated ring resonators on $\text{Al}_{0.1}\text{Ga}_{0.9}\text{N}$ nanomembranes transferred onto SiO_2/Si substrates. While their work demonstrated the versatility of AlGaIn, using nanomembranes introduces difficulties with handling and scalability. Recently, Shin et al. showcased the enhancement of the Pockels effect in multiple AlGaIn/AlN quantum wells on AlN due to the large built-in polarization of the quantum wells [47]. Despite encountering relatively high propagation losses (18.3 dB/cm), their work achieved a 20-fold increase in second-order susceptibility compared to bare AlN. This work shows the capability of the AlGaIn/AlN as a platform for cutting-edge engineering to achieve nonlinearities beyond those available in bulk materials.

Here, we develop heterogeneously grown AlGaIn into a photonic platform. To fabricate photonic devices, we grow $\text{Al}_x\text{Ga}_{1-x}\text{N}$, with $x = 0.69$, directly on high-temperature annealed AlN-on-sapphire templates with a reduced dislocation density [48]. Into this heterostructure, we subsequently fabricate the fundamental constituents of photonic integrated circuits with electron beam lithography and plasma etching: waveguides, directional couplers, ring resonators, and fiber couplers. Finally, we present the design of a device to achieve efficient and flexible phase matching for entangled photon generation using Spontaneous Parametric Down-Conversion (SPDC) at telecom wavelengths employing such a heterostructure.

II. RESULTS

A. Wafer Growth and Characterization

The core ingredient of our novel integrated photonics platform is an AlGaIn heterostructure (Fig. 2(b)). The AlN/AlGaIn layer stack is epitaxially grown on a c -plane-oriented sapphire substrate with an offset of 0.25° towards an m -plane. First, a 350 nm thick AlN layer is deposited using epitaxial magnetron sputtering. The sputtered material's threading dislocation density (TDD) was decreased through high-temperature annealing (HTA), following the process described by Miyake et al. [49]. During HTA, a temperature of 1700°C is maintained for a relatively short duration of 1h to prevent the formation of aluminum oxynitride on the AlN surface [32]. Subsequently, the rough sputtered and annealed surface is smoothed by MOVPE growth of 50 nm AlN in a step flow growth regime. The AlN layer, with a total thickness of 400 nm, exhibits a TDD of $7.5 \times 10^8 \text{ cm}^{-2}$, as estimated from high-resolution X-ray diffraction (HRXRD) measurements of the symmetric 0002 and skew-symmetric 10-12 ω -rocking-curves [50]. Atomic force microscopy (AFM) revealed a surface RMS roughness of 0.09 nm over a $25 \mu\text{m}^2$ area.

Next, a 250 nm thick AlGaIn waveguide layer is grown by MOVPE in a 6 x 2-inch close-coupled showerhead reactor on the AlN template, utilizing trimethylaluminum, triethylgallium, and ammonia as source materials, with hydrogen as the carrier gas, and a growth temperature of 1015°C . In-situ reflectometry measurements verify the

attainment of the targeted layer thickness of 250 nm. After AlGa_xN growth, we measure the surface RMS roughness by AFM to be 0.5 nm. This smooth surface supports integrating photonic devices as introduced here and enables the hetero-integration of superconducting nanowire single-photon detectors (SNSPDs) [14] and quantum devices. The strain relaxation towards the underlying AlN buffer and the Al-mole fraction x of the Al _{x} Ga_{1- x} N layers is determined by HRXRD using $\omega - \omega/2\theta$ reciprocal space maps (RSM) of the 11-24 reflection. Each RSM shows two sharp peaks (Fig. 2(a)), corresponding to the AlN template and AlGa_xN layers. By analyzing these data, an Al-mole fraction x of 0.69 and a relaxation of the in-plane compressive strain of only 3% can be determined for the AlGa_xN layer. This shows that the AlGa_xN grew almost pseudomorphically on the AlN template, and the generation of misfit dislocations for strain relief can thus be largely excluded.

B. Optical Material Properties

We use the prism coupling technique as described in [51, 52] to quantify the optical losses in the as-grown thin films. It utilizes a rutile prism to couple a tunable white laser (SuperK Fianium) into the heterostructures. The losses are quantified by monitoring the decay of the scattered light with a digital camera. We characterize and compare a 400 nm AlNoS sample and an AlGa_xN/AlN/sapphire wafer. The AlNoS supports a single TE₀ mode at 630 nm, whereas the AlGa_xN structure exhibits two distinct modes, TE₀ and TE₁, at the same wavelength. By fine-tuning the coupling angle, we isolate and analyze the losses of these modes, as reported in Fig. 2(d).

The TE₀ mode, in the AlGa_xN structure, exhibits optical losses that decrease with increasing wavelength, reaching a minimum value of 2.3 dB/cm above 600 nm. In contrast, the TE₁ mode of the AlGa_xN and the TE₀ mode of the AlNoS exhibited higher losses, with minimum values of approximately 5.9 and 4.3 dB/cm, respectively, which increase again for wavelengths over 625 nm. It is worth noting that both of these modes are localized at the interface between two different materials and, thus, are sensitive to the interface's inherent properties. Besides the roughness at the interface, additional sources of loss could be due to defects and color centers in AlN, which are presumably concentrated at the AlN-sapphire interface as shown by TEM measurements by [32–34]. AlN has defects comprising a mix of impurities, vacancies, and lattice defects. Factors like threading dislocations influence the formation of these defects, although the exact conditions for their formation are yet not fully understood [53–55].

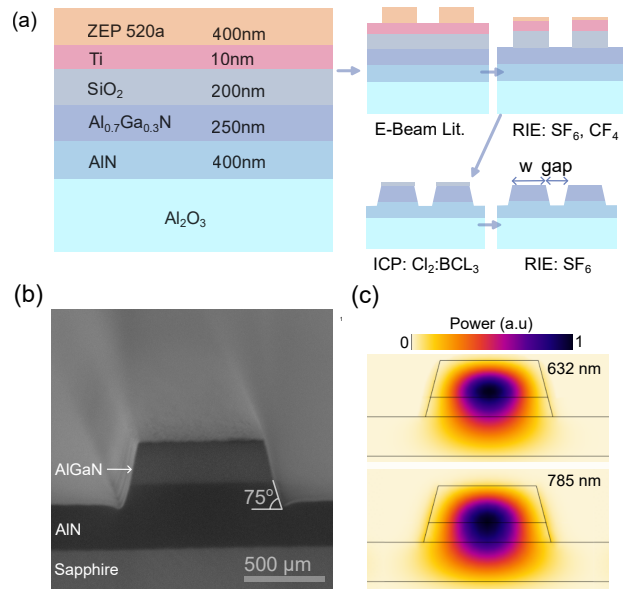


FIG. 3. **Fabrication geometries.** (a) Epitaxial and mask layers for the fabrication of the optical nanowaveguides. (b) SEM image of a cleaved facet of a waveguide, where the different materials can be clearly identified. (c) Simulated optical power distribution of the fundamental TE mode of the waveguides at 632 nm and 785 nm.

C. Device Fabrication

In the fabrication process of waveguides and ring resonators, we initially deposit a 200 nm thick SiO₂ layer using Plasma Enhanced Chemical Vapor Deposition (PECVD) to serve as a hard mask. We then coat a 10 nm thick Ti layer via e-beam evaporation to act as a charge dissipation layer, followed by 400 nm ZEP 520A e-beam lithography resist. The process steps are illustrated in Fig. 3(a). After patterning the resist, we transfer the pattern to the hard mask using a two-step reactive ion etching (RIE) process: we utilize SF₆ plasma to etch Ti and CF₄ plasma to etch SiO₂. In the final etching step, we process the AlGa_xN layer using BCl₃:Cl₂:He at a ratio of 10:50:10 sccm, under 600 W ICP power and 100 W RF power, at a pressure of 1 Pa. The AlGa_xN-to-SiO₂ etch rate ratio is approximately 3/1. We implement a laser-cut notch at the chip's edge to facilitate precise cleaving. Fig. 3(b) presents an SEM image of a cleaved facet, revealing the AlN and AlGa_xN layers. We measure the waveguides to have a wall angle of 75°. Fig. 3(c) shows the simulated power profiles of the fundamental TE mode of the waveguides at wavelengths of 632 nm and 785 nm. At the measurement wavelength of 785 nm used for our ring resonators, 90% of the optical power is located above the AlN-sapphire interface. At a shorter wavelength of 632 nm, this number increases to 95%, indicating that most of the optical power is well separated from the lossy boundary at the sapphire interface.

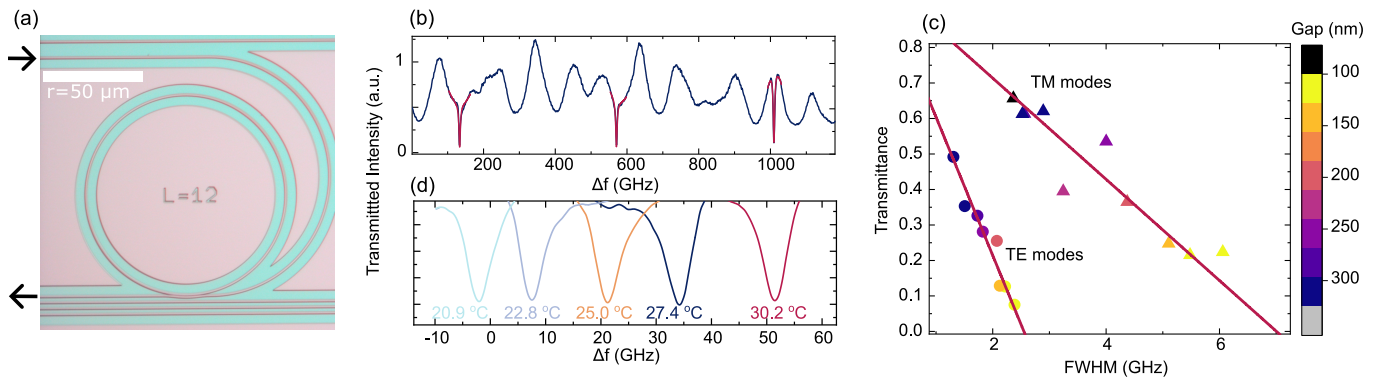


FIG. 4. **Ring resonator and waveguide device characterization.** (a) Optical microscope image of a waveguide coupled ring resonator. (b) The transmission through a ring resonator, with a width of 580 nm and a 100 nm coupling gap, is plotted as a function of laser detuning. The dark red lines represent fits using a Lorentzian function with a quadratic baseline. (c) The graph of transmittance versus the full width at half maximum (FWHM) of resonances for different coupling gaps between the semi-racetrack waveguide and the ring. The red lines represent linear fits for TE and TM modes. (d) The resonance frequency tuning with temperature.

D. Tunable Microring Resonators

We fabricate microring resonators with a radius of 50 μm and a top width of 580 nm, coupled to racetrack waveguides with the same width and cleaved at both ends, as depicted in Fig. 4(a). The sample is mounted on a 3D piezoelectric nanopositioner (Physik Instrumente, NanoCube) and characterized with a custom-made inverted microscope, where the same objective (Zeiss, LD EC Epiplan-Neofluar, 20X, NA = 0.22) is used to launch the laser light into the input waveguide facet and collect it from the output one. The alignment of the incoupling light is monitored with an EMCCD camera (Andor, iXon Ultra 897) and optimized by maximizing the intensity of the outcoupled signal by adjusting both sample position and laser incoupling angle. Propagation losses are then inferred by measuring the intrinsic quality factor of the microring resonators. To reach critical coupling, which allows for the estimation of resonator losses, we fabricate several microring resonators coupled to racetrack waveguides with different coupling gaps, ranging from 100 to 325 nm, as displayed in Fig. 4(c). We measure the transmission of a tunable 785 nm laser (Toptica, DFB PRO centered at 784.6 nm, MHF over 2 nm) and use a linear film polarizer (Thorlabs, LPVIS) to excite and collect TE or TM modes selectively. Fig. 4(b) illustrates the typical transmission as a function of the laser's frequency, with a baseline primarily attributed to the interference in measurement optics. This modulation can be described with a quadratic baseline from which the resonant peaks can be discriminated and fitted with a Lorentzian function, as indicated in red in Fig. 4(b). We extrapolate the resonance widths at the critical coupling, i.e., zero transmittance. The key parameters, such as the critical coupling FWHM, free spectral ranges (FSRs), and intrinsic Q-factors for TE and TM modes, are summarized in Table I.

TABLE I. Summary of the measured and calculated optical and thermo-optic parameters for the $\text{Al}_x\text{Ga}_{1-x}\text{N}$ ($x=0.69$) ring resonators with 50 μm radius.

Parameter	TE	TM
FWHM at Critical Coupling (GHz)	2.5	7.0
FSR (GHz)	438	426
Propagation loss (dB/cm)	2.5	7.1
Intrinsic Q factor	1.5×10^5	0.55×10^5
$d\nu/dT$ at 785 nm (GHz/K)	5.7	6.2
dn/dT ($\times 10^{-5} \text{ K}^{-1}$)	2.9	3.26
n_{AlGa_N} at 632 nm	2.13	2.19
n_{AlN} at 632 nm	2.05	2.10

We mount the chips on a custom-made temperature-controlled stage to test the temperature tunability of the TE and TM modes resonance frequencies in the range of 20-30 $^\circ\text{C}$. Fig. 4(c) depicts the shift of a resonant peak of the TE mode (coupling gap=100nm) for different temperatures. In the investigated temperature range, the central frequency of the resonance changes linearly with temperature. The corresponding temperature coefficients are 5.7 and 6.2 GHz/K for TE and TM modes, respectively. These coefficients correspond to a thermo-optic coefficient of $2.9 \times 10^{-5} \text{ K}^{-1}$ and $3.6 \times 10^{-5} \text{ K}^{-1}$ for TE and TM polarizations in the AlGa_N waveguide, which is comparable to the previously reported values for AlN ($2.94 \times 10^{-5} \text{ K}^{-1}$) and GaN ($7.01 \times 10^{-5} \text{ K}^{-1}$) [56] at 785 nm and 300K.

E. Directional Couplers

Directional couplers are essential components in photonic integrated circuits. They enable the transfer of electromagnetic energy between two or more waveguides that are in proximity. They can be combined to form

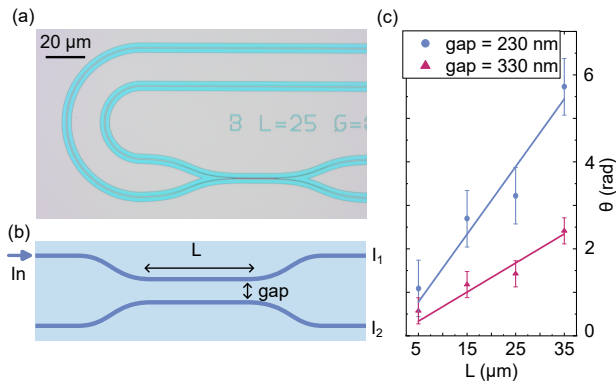


FIG. 5. **Directional couplers.** (a) Optical microscope image of an AlGaIn directional coupler. (b) Schematic illustration of the geometry, where the relevant parameters are presented. (c) Output intensity ratios, Θ , across various coupling lengths and gap sizes, enabling the determination of the coupling constant for gaps measuring 230 and 330 nm.

optical switches or Mach-Zehnder interferometers, which are the fundamental constituents of most on-chip quantum technology applications [57, 58]. In our study, we develop AlGaIn directional couplers linked to racetrack waveguides, as depicted in Fig. 5(a). We vary coupling gaps and lengths, as illustrated in Fig. 5(b). By injecting a 632 nm laser into one of the input ports, we measure the output intensity ratio: $\theta = \tan^{-1}(I_1/I_2)$. Our observations reveal a direct linear correlation between the coupling length and θ , with linear fitting of the data providing the coupling constants. For coupling gaps of 230 nm and 330 nm, the coupling constants were determined to be $0.15 \mu\text{m}^{-1}$ and $0.066 \mu\text{m}^{-1}$, respectively. The observed uncertainties are primarily attributed to reflections at the input and output facets, which can be minimized by applying an anti-reflection coating. The well-functioning directional couplers show that our AlGaIn platform is well-suited for building the required components of complex integrated photonic circuits. Further improvement is to be expected by optimizing the etching processes towards vertical sidewalls.

F. Phase Matching for Nonlinear Frequency Conversion and Pair Generation

In nonlinear photonics applications, achieving a phase matching of the modes involving the nonlinear conversion process is critical for efficiency. For integrated photonic waveguides, a common strategy is to match the effective indices of two distinct modes, typically a fundamental mode and a higher order mode [43, 59]. These approaches, however, suffer from a weak overlap between the involved modes. The mode overlap integral for second harmonic generation and SPDC for degenerate pho-

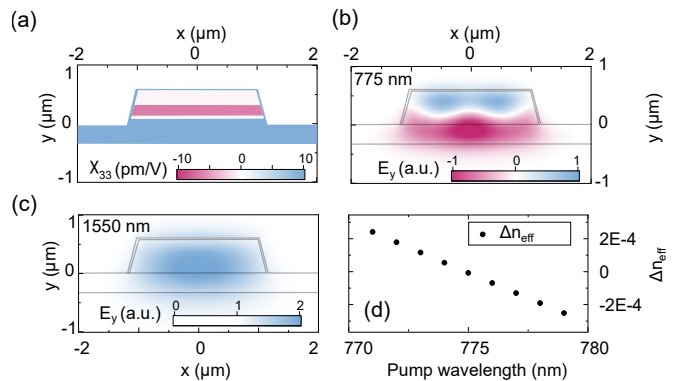


FIG. 6. **Phase matching for SPDC.** An optimized heterostructure of $\text{Al}_x\text{Ga}_{1-x}\text{N}$ for entangled photon pair generation at 1550 nm. (a) Second-order nonlinear susceptibility tensor element χ_{33} , (b) vertical component of the electric field of the higher order TM mode at 775 nm, (c) the fundamental TM mode at 1550 nm, and (d) effective index difference between these two modes as a function of pump laser wavelength.

ton pairs is defined as [60]

$$\Gamma = \left| \int \chi^{(2)} : \mathbf{E}_\omega^2 \mathbf{E}_{2\omega}^* d\Omega \right|, \quad (1)$$

where $\chi^{(2)}$ is the second-order nonlinear susceptibility tensor, \mathbf{E}_ω and $\mathbf{E}_{2\omega}$ are the normalized mode electric field amplitudes of the modes at ω and 2ω , respectively. The integral is calculated over the mode volume Ω . In the case of phase-matched TM modes for AlGaIn waveguides, the dominating term in the overlap integral is

$$\Gamma \approx \left| \int \chi_{33} E_{1y}^2 E_{2y}^* dx dy \right|, \quad (2)$$

where χ_{33} is the relevant component of $\chi^{(2)}$ for the interaction along the primary axis of the crystal in TM modes, and E_{1y} and E_{2y} are the y-components of the electric field amplitudes. $\text{Al}_x\text{Ga}_{1-x}\text{N}$ alloys exhibit a sign change of the second-order nonlinear coefficient tensor component (χ_{33}) at an alloy content of approximately $x = 0.65$ [41]. We use this property to enhance the mode overlap. We design a heterostructure to achieve phase matching between the fundamental TM mode at 1550 nm and a higher-order mode at 775 nm with identical polarization, as demonstrated in Fig. 6(a-c). This strategy facilitates efficient phase matching, enabled by the sign change of χ_{33} , which significantly increases the overlap integral between the pump and SPDC modes. Our concept also allows for fine-tuning phase matching by adjusting the pump wavelength. The resultant effective index difference, Δn_{eff} , between the pump and down-conversion modes, which converge to zero at approximately 775 nm, is depicted in Fig. 6(d). For this simulation, we used a finite element solver (Comsol Multiphysics) to calculate the modes' effective indices and used a genetic algorithm (supplied by Matlab) to minimize the objective

function, $(10^2 \Delta n_{eff} - \Gamma)$. From bottom to top, optimized AlGaIn layer thicknesses are 110/70/290/50 nm on 400 nm AlN on sapphire, while the alloy compositions are 0.55/0.42/0.65/0.66. The waveguide's top width is 1.98 μm , and the AlN layer is over-etched to a depth of 60 nm. Additionally, we define a 30 nm conformal AlN cladding. This particular layer design will likely exhibit some degree of strain relaxation, especially in the layers with low Al content. Changes in strain and piezoelectric polarization may impact the alignment of this calculation with experimental results. However, the overall viability of this method remains unaffected. The AlGaIn/AlN heterostructure concept enables the engineering of compact SPDC sources and phase-matched ring resonators across a wide spectral range when coupled to a single-mode waveguide in a ring waveguide.

III. DISCUSSION

We present a new material platform based on AlGaIn heterostructures, which can be used to implement photonic devices with the core functionalities required to develop advanced photonic integrated chips. By epitaxially growing AlGaIn on HTA-AlN templates on sapphire substrates, we alleviate the challenges related to crystal defects and dislocations at the sapphire-AlN interface and achieved an RMS surface roughness as low as 0.5 nm. The optical losses we quantify, 2.5 dB/cm for TE₀ mode and 7.1 dB/cm for TM₀ mode at 785 nm, outperform earlier measurements on aluminum nitride on sapphire waveguides in the visible spectrum. For instance, Lu et al. found losses of 5.3 dB/cm at 633 nm for the TE₀ mode [61]. It is worth noting that we did not use a cladding material, which typically helps to reduce scattering loss further. By optimizing the layer sequence and growth recipes, as well as device fabrication, further reduction of losses will be possible. Moreover, by measuring the thermo-optic coefficient and anisotropic refractive indices of the waveguides, we have gained insight into parameters relevant to applications such as nonlinear photon-pair generation and on-chip nonlinear conversion. The birefringent refractive index of our devices opens avenues for exploration, especially in its utilization for phase matching of TE and TM modes. Furthermore, the surface

roughness of the epitaxial material is sufficiently low to integrate superconducting single-photon detectors [62]. Our work introduces AlGaIn heterostructures as a novel platform for integrated photonics, offering a scalable and high-quality alternative to well-established materials.

ACKNOWLEDGMENTS

We thank Torsten Petzke and Cornelia Neumann for assistance in AlGaIn growth, Karina Ickert and Nico Sluka for their help in spin-coating and lithography, Joost Wartena, Adrian Runge, Mohammad Mohammadi, and Dominik Sudau for their assistance in thin-film depositions; Kevin Kunkel, Natalia Sabelfeld, Kai Gehrke, and Andreas Renkewitz for performing plasma etching processes; Alexander Külberg and Felix Eiche for laser cutting and marking; Uwe Spengler and Christine Münnich for cleaving, Olaf Krüger, Ralph-Stephan Unger and Ina Ostermay for fruitful discussions. We also thank Professor Arno Rauschenbetuel for providing access to his laboratory and the ring resonator measurement resources. This work received support from the European Research Council (ERC), Starting Grant project QUREP, No. 851810, the German Federal Ministry of Education and Research (BMBF, project DiNOQuant, No. 13N14921; project QPIS, No. 16KISQ032K; project QPIC-1, No. 13N15858), the Einstein Foundation Berlin (Einstein Research Unit: Perspectives of a quantum digital transformation: Near-term quantum computational devices and quantum processors), and Alexander von Humboldt Foundation in the framework of the Alexander von Humboldt Professorship endowed by the BMBF.

CONTRIBUTIONS

S.G. led microfabrication, characterization, simulations, and manuscript writing; S.P. specialized in ring resonator characterization; T.P. conducted e-beam lithography and supervised the fabrication processes; T.K. and S.H. were responsible for AlGaIn material growth, M.W. and T.S. led the project. All authors reviewed the manuscript.

-
- [1] B. J. Shastri, A. N. Tait, T. Ferreira de Lima, W. H. P. Pernice, H. Bhaskaran, C. D. Wright, and P. R. Prucnal, Photonics for artificial intelligence and neuromorphic computing, *Nature Photonics* **15**, 102–114 (2021).
- [2] J. Xavier, D. Yu, C. Jones, E. Zossimova, and F. Vollmer, Quantum nanophotonic and nanoplasmonic sensing: towards quantum optical bioscience laboratories on chip, *Nanophotonics* **10**, 1387 (2021).
- [3] C. M. Knaut, A. Suleymanzade, Y.-C. Wei, D. R. Assumpcao, P.-J. Stas, Y. Q. Huan, B. Machielse, E. N.

- Knall, M. Sutula, G. Baranes, N. Sinclair, C. De-Eknamkul, D. S. Levonian, M. K. Bhaskar, H. Park, M. Lončar, and M. D. Lukin, Entanglement of nanophotonic quantum memory nodes in a telecommunication network (2023), arXiv:2310.01316.
- [4] G. Zhang, J. Y. Haw, H. Cai, F. Xu, S. M. Assad, J. F. Fitzsimons, X. Zhou, Y. Zhang, S. Yu, J. Wu, W. Ser, L. C. Kwek, and A. Q. Liu, An integrated silicon photonic chip platform for continuous-variable quantum key distribution, *Nature Photonics* **13**, 839–842 (2019).

- [5] J. Borregaard, H. Pichler, T. Schröder, M. D. Lukin, P. Lodahl, and A. S. Sørensen, One-way quantum repeater based on near-deterministic photon-emitter interfaces, *Physical Review X* **10**, 10.1103/physrevx.10.021071 (2020).
- [6] G. Pieplow, Y. Strocka, M. Isaza-Monsalve, J. H. D. Munns, and T. Schröder, Deterministic creation of large photonic multipartite entangled states with group-IV color centers in diamond (2023), arXiv:2312.03952.
- [7] L. Orphal-Kobin, C. G. Torun, J. M. Bopp, G. Pieplow, and T. Schröder, Coherent microwave, optical, and mechanical quantum control of spin qubits in diamond (2023), arXiv:2312.06431.
- [8] Y. Liu, K. Xu, S. Wang, W. Shen, H. Xie, Y. Wang, S. Xiao, Y. Yao, J. Du, Z. He, and Q. Song, Arbitrarily routed mode-division multiplexed photonic circuits for dense integration, *Nature Communications* **10**, 10.1038/s41467-019-11196-8 (2019).
- [9] Z. Zeng, L. Lu, P. He, D. Liu, and M. Zhang, Demonstration of dual-mode photonic integrated circuit based on inverse-designed photonic components, *IEEE Photonics Technology Letters* **33**, 1289 (2021).
- [10] S. Y. Siew, B. Li, F. Gao, H. Y. Zheng, W. Zhang, P. Guo, S. W. Xie, A. Song, B. Dong, L. W. Luo, C. Li, X. Luo, and G.-Q. Lo, Review of silicon photonics technology and platform development, *Journal of Lightwave Technology* **39**, 4374–4389 (2021).
- [11] A. D. Logan, M. Gould, E. R. Schmidgall, K. Hestoffer, Z. Lin, W. Jin, A. Majumdar, F. Hatami, A. W. Rodriguez, and K.-M. C. Fu, 400%/W second harmonic conversion efficiency in 14 μm -diameter gallium phosphide-oxide resonators, *Optics Express* **26**, 33687 (2018).
- [12] X. Guo, C.-I. Zou, C. Schuck, H. Jung, R. Cheng, and H. X. Tang, Parametric down-conversion photon-pair source on a nanophotonic chip, *Light: Science & Applications* **6**, e16249 (2016).
- [13] X. Wang, X. Jiao, B. Wang, Y. Liu, X.-P. Xie, M.-Y. Zheng, Q. Zhang, and J.-W. Pan, Quantum frequency conversion and single-photon detection with lithium niobate nanophotonic chips, *npj Quantum Information* **9** (2023).
- [14] D. Zhu, H. Choi, T.-J. Lu, Q. Zhao, A. Dane, F. Najafi, D. R. Englund, and K. K. Berggren, Superconducting nanowire single-photon detector on aluminum nitride, in *2016 Conference on Lasers and Electro-Optics (CLEO)* (2016) pp. 1–2.
- [15] I. Esmaeil Zadeh, J. Chang, J. W. N. Los, S. Gyger, A. W. Elshaari, S. Steinhauer, S. N. Dorenbos, and V. Zwiller, Superconducting nanowire single-photon detectors: A perspective on evolution, state-of-the-art, future developments, and applications, *Applied Physics Letters* **118** (2021).
- [16] S. L. Mouradian, T. Schröder, C. B. Poitras, L. Li, J. Goldstein, E. H. Chen, M. Walsh, J. Cardenas, M. L. Markham, D. J. Twitchen, M. Lipson, and D. Englund, Scalable Integration of Long-Lived Quantum Memories into a Photonic Circuit, *Phys. Rev. X* **5**, 031009 (2015).
- [17] T. Pregnolato, M. E. Stucki, J. M. Bopp, M. H. v. d. Hoeven, A. Gokhale, O. Krüger, and T. Schröder, Fabrication of sawfish photonic crystal cavities in bulk diamond, *APL Photonics* **9**, 10.1063/5.0186509 (2024).
- [18] G. Poberaj, H. Hu, W. Sohler, and P. Günter, Lithium niobate on insulator (LNOI) for micro-photonic devices, *Laser & Photonics Reviews* **6**, 488 (2012).
- [19] Y. Qi and Y. Li, Integrated lithium niobate photonics, *Nanophotonics* **9**, 1287–1320 (2020).
- [20] S. Saravi, T. Pertsch, and F. Setzpfandt, Lithium niobate on insulator: An emerging platform for integrated quantum photonics, *Advanced Optical Materials* **9** (2021).
- [21] D. Zhu, L. Shao, M. Yu, R. Cheng, B. Desiatov, C. J. Xin, Y. Hu, J. Holzgrafe, S. Ghosh, A. Shams-Ansari, E. Puma, N. Sinclair, C. Reimer, M. Zhang, and M. Lončar, Integrated photonics on thin-film lithium niobate, *Adv. Opt. Photonics* **13**, 242 (2021).
- [22] X. Han, M. Yuan, H. Xiao, G. Ren, T. G. Nguyen, A. Boes, Y. Su, A. Mitchell, and Y. Tian, Integrated photonics on the dielectrically loaded lithium niobate on insulator platform, *Journal of the Optical Society of America B* **40**, D26 (2023).
- [23] B. Zivasatienraj, M. B. Tellekamp, and W. A. Doolittle, Epitaxy of LiNbO₃: Historical challenges and recent success, *Crystals* **11**, 397 (2021).
- [24] K. A. Buzaverov, A. S. Baburin, E. V. Sergeev, S. S. Avdeev, E. S. Lotkov, M. Andronik, V. E. Stukalova, D. A. Baklykov, I. V. Dyakonov, N. N. Skryabin, M. Y. Saygin, S. P. Kulik, I. A. Ryzhikov, and I. A. Rodionov, Low-loss silicon nitride photonic ICs for near-infrared wavelength bandwidth, *Optics Express* **31**, 16227 (2023).
- [25] A. Hermans, M. V. Daele, J. Dendooven, S. Clemmen, C. Detavernier, and R. Baets, Integrated silicon nitride electro-optic modulators with atomic layer deposited overlays, *Opt. Lett.* **44**, 1112 (2019).
- [26] H. Nejadriahi, A. Friedman, R. Sharma, S. Pappert, Y. Fainman, and P. Yu, Thermo-optic properties of silicon-rich silicon nitride for on-chip applications, *Opt. Express* **28**, 24951 (2020).
- [27] N. Li, C. P. Ho, S. Zhu, Y. H. Fu, Y. Zhu, and L. Y. T. Lee, Aluminium nitride integrated photonics: a review, *Nanophotonics* **10**, 2347–2387 (2021).
- [28] Y. Sun, W. Shin, D. A. Laleyan, P. Wang, A. Pandey, X. Liu, Y. Wu, M. Soltani, and Z. Mi, Ultrahigh Q microring resonators using a single-crystal aluminum-nitride-on-sapphire platform, *Optics Letters* **44**, 5679 (2019).
- [29] X. Wu, J. Feng, X. Liu, , and H. Zeng, Effects of rapid thermal annealing on aluminum nitride waveguides, *Optical Materials Express* **10**, 10.1364/OME.410129 (2020).
- [30] X. Liu, A. W. Bruch, Z. Gong, J. Lu, J. B. Surya, L. Zhang, J. Wang, J. Yan, and H. X. Tang, Ultra-high-Q UV microring resonators based on a single-crystalline AlN platform, *Optica* **5**, 1279 (2018).
- [31] X. Liu, C. Sun, B. Xiong, L. Wang, J. Wang, Y. Han, Z. Hao, H. Li, Y. Luo, J. Yan, T. Wei, Y. Zhang, and J. Wang, Aluminum nitride-on-sapphire platform for integrated high-Q microresonators, *Opt. Express* **25**, 587 (2017).
- [32] S. Hagedorn, S. Walde, A. Mogilatenko, M. Weyers, L. Cancellara, M. Albrecht, and D. Jaeger, Stabilization of sputtered AlN/sapphire templates during high temperature annealing, *Journal of Crystal Growth* **512**, 142 (2019).
- [33] Y. Tokumoto, N. Shibata, T. Mizoguchi, T. Yamamoto, and Y. Ikuhara, Atomic structure of threading dislocations in AlN thin films, *Physica B: Condensed Matter* **404**, 4886 (2009).
- [34] E. Dogheche, B. Belgacem, D. Remiens, P. Ruterana, and F. Omnes, Prism coupling as a non-destructive tool for optical characterization of (Al, Ga) nitride compounds,

- MRS Internet Journal of Nitride Semiconductor Research **5**, 747 (2000).
- [35] U. T. Schwarz, E. Sturm, W. Wegscheider, V. Kümmler, A. Lell, and V. Härle, Excitonic signature in gain and carrier induced change of refractive index spectra of (In, Al)GaN quantum well lasers, *Applied Physics Letters* **85**, 1475 (2004).
- [36] C. Bulutay, C. M. Turgut, and N. A. Zakhleniuk, Carrier-induced refractive index change and optical absorption in wurtzite InN and GaN: Full-band approach, *Physical Review B* **81**, 10.1103/physrevb.81.155206 (2010).
- [37] A. Udabe, I. Baraia-Etxaburu, and D. G. Diez, Gallium nitride power devices: A state of the art review, *IEEE Access* **11**, 48628 (2023).
- [38] T. A. Tabbakh, D. Anandan, M. J. Sheldon, P. Tyagi, and A. Alfaifi, Recent advancements in GaN LED technology, in *Light-Emitting Diodes - New Perspectives* (IntechOpen, 2023).
- [39] F. Liang, D. Zhao, Z. Liu, P. Chen, J. Yang, L. Duan, Y. Shi, and H. Wang, GaN-based blue laser diode with 6.0 W of output power under continuous-wave operation at room temperature, *Journal of Semiconductors* **42**, 112801 (2021).
- [40] L. Hu, X. Ren, J. Liu, A. Tian, L. Jiang, S. Huang, W. Zhou, L. Zhang, and H. Yang, High-power hybrid GaN-based green laser diodes with ITO cladding layer, *Photonics Research* **8**, 279 (2020).
- [41] N. A. Sanford, A. V. Davydov, D. V. Tsvetkov, A. V. Dmitriev, S. Keller, U. K. Mishra, S. P. DenBaars, S. S. Park, J. Y. Han, and R. J. Molnar, Measurement of second order susceptibilities of GaN and AlGaIn, *Journal of Applied Physics* **97**, 053512 (2005).
- [42] J. Chen, Z. H. Levine, and J. W. Wilkins, Calculated second-harmonic susceptibilities of BN, AlN, and GaN, *Applied Physics Letters* **66**, 1129–1131 (1995).
- [43] F. D. Leonardis, R. A. Soref, M. Soltani, and V. M. N. Passaro, Broadband biphoton generation and statistics of quantum light in the UV-visible range in an AlGaIn microring resonator, *Scientific Reports* (2017).
- [44] F. D. Leonardis, R. A. Soref, M. Soltani, and V. M. Passaro, Stimulated Brillouin scattering in an AlGaIn photonics platform operating in the visible spectral range, *Scientific Reports* **8**, 10.1038/S41598-018-33183-7 (2018).
- [45] N. Li, I. Waki, C. Kumtornkittikul, J. H. Liang, M. Sugiyama, Y. Shimogaki, and Y. Nakano, Fabrication of AlGaIn-based waveguides by inductively coupled plasma etching, *Japanese Journal of Applied Physics, Part 2: Letters* **43**, 10.1143/JJAP.43.L1340 (2004).
- [46] A. W. Bruch, K. Xiong, H. Jung, X. Guo, C. Zhang, J. Han, and H. X. Tang, Electrochemically sliced low loss AlGaIn optical microresonators, *Applied Physics Letters* **110**, 10.1063/1.4973521 (2017).
- [47] W. J. Shin, P. Wang, Y. Sun, S. Paul, J. Liu, M. Kira, M. Soltani, and Z. Mi, Enhanced pockels effect in aln microring resonator modulators based on AlGaIn/AlN multiple quantum wells, *ACS Photonics* **10**, 34 (2023).
- [48] S. Hagedorn, S. Walde, A. Knauer, N. Susilo, D. Pacak, L. Cancellara, C. Netzel, A. Mogilatenko, C. Hartmann, T. Wernicke, M. Kneissl, and M. Weyers, Status and prospects of AlN templates on sapphire for ultraviolet light-emitting diodes, *physica status solidi (a)* **217**, 10.1002/pssa.201901022 (2020).
- [49] H. Miyake, C.-H. Lin, K. Tokoro, and K. Hiramatsu, Preparation of high-quality AlN on sapphire by high-temperature face-to-face annealing, *Journal of Crystal Growth* **456**, 155 (2016).
- [50] B. N. Pantha, R. Dahal, M. L. Nakarmi, N. Nepal, J. Li, J. Y. Lin, H. X. Jiang, Q. S. Paduano, and D. Weyburne, Correlation between optoelectronic and structural properties and epilayer thickness of AlN, *Applied Physics Letters* **90**, 10.1063/1.2747662 (2007).
- [51] H. P. Weber, F. A. Dunn, and W. N. Leibolt, Loss measurements in thin-film optical waveguides, *Appl. Opt.* **12**, 755 (1973).
- [52] E. Dogheche, D. Rémiens, A. Boudrioua, and J. C. Loulengue, Growth and optical characterization of aluminum nitride thin films deposited on silicon by radio-frequency sputtering, *Applied Physics Letters* **74**, 1209 (1999).
- [53] J. K. Cannon, S. G. Bishop, J. P. Hadden, H. B. Yağcı, and A. J. Bennett, Polarization study of single color centers in aluminum nitride, *Applied Physics Letters* **122**, 10.1063/5.0145542 (2023).
- [54] J. B. Varley, A. Janotti, and C. G. V. de Walle, Defects in AlN as candidates for solid-state qubits, *Physical Review B* **93**, 10.1103/physrevb.93.161201 (2016).
- [55] Y. Xue, J. Yuan, Q. Li, F. Chen, X. Yuan, Z. Ju, S. Zhang, B. Wu, Y. Hou, M. Li, J. Zhang, and E. Wu, Deciphering the photophysical properties of near-infrared quantum emitters in AlGaIn films by transition dynamics, *Nanoscale* **14**, 18115 (2022).
- [56] N. Watanabe, T. Kimoto, and J. Suda, The temperature dependence of the refractive indices of GaN and AlN from room temperature up to 515 °C, *Journal of Applied Physics* **104**, 10.1063/1.3021148 (2008).
- [57] H. Zhou, J. Dong, J. Cheng, W. Dong, C. Huang, Y. Shen, Q. Zhang, M. Gu, C. Qian, H. Chen, Z. Ruan, and X. Zhang, Photonic matrix multiplication lights up photonic accelerator and beyond, *Light: Science & Applications* **11**, 10.1038/s41377-022-00717-8 (2022).
- [58] W. R. Clements, P. C. Humphreys, B. J. Metcalf, W. S. Kolthammer, and I. A. Walmsley, Optimal design for universal multiport interferometers, *Optica* **3**, 1460 (2016).
- [59] W. H. Pernice, C. Xiong, C. Schuck, and H. X. Tang, Second harmonic generation in phase matched aluminum nitride waveguides and micro-ring resonators, *Applied Physics Letters* **100**, 10.1063/1.4722941 (2012).
- [60] A. Noor, A. R. Damodaran, I.-H. Lee, S. A. Maier, S.-H. Oh, and C. Ciraci, Mode-matching enhancement of second-harmonic generation with plasmonic nanopatch antennas, *ACS Photonics* **7**, 3333 (2020), pMID: 33365359.
- [61] T.-J. Lu, M. Fanto, H. Choi, P. Thomas, J. Steidle, S. Mouradian, W. Kong, D. Zhu, H. Moon, K. Berggren, J. Kim, M. Soltani, S. Preble, and D. Englund, Aluminum nitride integrated photonics platform for the ultraviolet to visible spectrum, *Opt. Express* **26**, 11147 (2018).
- [62] R. Flaschmann, C. Schmid, L. Zugliani, S. Strohauser, F. Wietschorke, S. Grotowski, B. Jonas, M. Müller, M. Althammer, R. Gross, J. J. Finley, and K. Müller, Optimizing the growth conditions of Al mirrors for superconducting nanowire single-photon detectors, *Materials for Quantum Technology* **3**, 035002 (2023).